Characterizing pore-scale structure-flow correlations in sedimentary rocks using magnetic resonance imaging

K. Karlsons ●,[1] D. W. de Kort ●,[1,2,*] A. J. Sederman ●,[1] M. D. Mantle ●,[1] J. J. Freeman ●,[3] M. Appel ●,[2] and L. F. Gladden ●[1]

[1]*Magnetic Resonance Research Centre, Department of Chemical Engineering and Biotechnology, University of Cambridge, Philippa Fawcett Drive, Cambridge CB3 0AS, United Kingdom*

[2]*Shell Technology Centre Amsterdam, Shell Global Solutions International B.V., Grasweg 31, 1031 HW Amsterdam, the Netherlands*

[3]*Shell Technology Center Houston, Shell Exploration and Production Inc., 3333 Highway 6 S, Houston, Texas 77082, USA*

Quantitative, three-dimensional (3D) spatially resolved magnetic resonance flow imaging (flow MRI) methods are presented to characterize structure-flow correlations in a 4-mm-diameter plug of Ketton limestone rock using undersampled **k**- and **q**-space data acquisition methods combined with compressed sensing (CS) data reconstruction techniques. The acquired MRI data are coregistered with an X-ray microcomputed tomography (μCT) image of the same rock sample, allowing direct correlation of the structural features of the rock with local fluid transport characteristics. First, 3D velocity maps acquired at 35 μm isotropic spatial resolution showed that the flow was highly heterogeneous, with $\sim$10% of the pores carrying more than 50% of the flow. Structure-flow correlations were found between the local flow velocities through pores and the size and topology (coordination number) associated with these pores. These data show consistent trends with analogous data acquired for flow through a packing of 4-mm-diameter spheres, which may be due to the microstructure of Ketton rock being a consolidation of approximately spherical grains. Using two-dimensional and 3D visualization of coregistered μCT images and velocity maps, complex pore-scale flow patterns were identified. Second, 3D spatially resolved propagators were acquired at 94 μm isotropic spatial resolution. Flow dispersion within the rock was examined by analyzing each of the 331 776 local propagators as a function of observation time. Again, the heterogeneity of flow within the rock was shown. Quantification of the mean and standard deviation of each of the local propagators showed enhanced mixing occurring within the pore space at longer observation times. These spatially resolved measurements also enable investigation of the length scale of a representative elementary volume. It is shown that for a 4-mm-diameter plug this length scale is not reached.

I. INTRODUCTION

Analytical and imaging techniques that can help visualize fluid transport phenomena in the pore space of sedimentary rocks are of significant interest for the oil and gas industry. In the face of a growing global energy consumption, and at the same time an urgent need to reduce pressure on the environment, enhanced oil recovery (EOR) and carbon capture and sequestration (CCS) may be part of a future in which hydrocarbons are produced in a more sustainable manner. Through EOR, more hydrocarbons can be sourced from a single well by injection of brine, polymers, or surfactants, thereby reducing the need for additional drilling. In CCS, carbon dioxide is reinjected into a reservoir so that it does not enter the atmosphere. Fluid flow through rock also drives the process of geothermal heat extraction, which is a promising source of renewable energy. Advanced laboratory-based analytical and imaging techniques play a key role in the fine-tuning and deployment of such subsurface technologies.

Driven by the development of powerful, high-resolution three-dimensional (3D) imaging and petrophysical modeling capabilities, Digital Rock (DR) technology [1–5] is emerging as a tool to predict petrophysical properties of rock samples on the basis of segmented high-resolution 3D images of the pore space. DR technology aims to augment conventional characterization of sedimentary rocks, which is based on measurements of macroscopic petrophysical properties of a whole core plug sample. Although these macroscopic, or bulk, properties are critical to any petrophysical analysis, they provide little insight into the degree of spatial variation of these properties. However, heterogeneity in petrophysical properties is a key factor underlying the efficiency of hydrocarbon recovery processes. X-ray microcomputed tomography (μCT) is currently the primary tool for obtaining structural images of the rock matrix [1,4,5], and such images are routinely acquired on the micron scale. It remains necessary, however, to validate, initialize, and calibrate DR simulations on the basis of laboratory measurements that also capture the spatial variation in petrophysical properties within the rock. As shown in this paper, the high-resolution magnetic resonance imaging (MRI) techniques demonstrated are well placed to do this. These MRI data can ultimately be used to validate the prediction of the simulators.

MRI has been widely used to study porous materials, including porous rock core plugs, because it provides a direct

_____
*Corresponding author: dd487@cam.ac.uk

and noninvasive way to obtain quantitative chemical [6,7], microstructural [8,9], and transport-related [10–14] information within optically opaque materials saturated with fluid. Due to the relatively low sensitivity of the magnetic resonance (MR) method, such MRI data are typically acquired at spatial resolutions on the order of a few hundred microns. However, the pore sizes in sedimentary rocks are typically smaller than 100 μm and therefore there has been a strong motivation to increase the spatial resolution of MRI measurements to be able to obtain local structure-transport correlations at spatial resolutions similar to that of the relevant pore scale.

The present work therefore utilizes a set of MRI methods to obtain quantitative, 3D spatially resolved information about fluids in rocks at a pore-scale resolution. It has recently been demonstrated that by using rapid, compressed sensing (CS) MRI [15], it is possible to acquire 3D MRI images of carbonate rocks at a spatial resolution of 17.6 μm [8], which is at least an order of magnitude higher than the resolution of conventional MRI, and is a resolution at which pore-scale features in many rocks can be clearly discerned. In this work, this approach has been extended to include quantitative image contrast and hence the ability to extract structure-flow correlations at the pore scale. More specifically, fluid displacements were encoded into the images under single-phase flow conditions. Two types of displacement measurements were performed. Velocity maps give a single-value measurement of the average fluid velocity within each voxel of the image. In contrast, spatially resolved displacement propagators give a probability distribution of fluid displacements over a given observation time for each voxel within the image and are used to study the effects of molecular self-diffusion and flow dispersion within the pores. It is shown that through coregistration of the resulting flow data with μCT images, which have an order-of-magnitude higher spatial resolution, the details of the flow distribution can be correlated with the microstructural features of the rock.

The flow MRI methods are used to characterize flow within Ketton limestone, using a cylindrical mini-plug with a diameter of 4 mm. Ketton limestone is an outcrop rock and a widely used model system in imaging studies of porous rocks [8,16,17]. Ketton rock is oolytic in nature: it consists of layered, microporous spherical grains (ooids) packed closely together. The rock therefore has micropores within the grains and macropores between the grains.

II. PORE-SCALE FLOW MRI

Based on rapid, compressed sensing MRI methods demonstrated in our previous works [8,13,18], new MRI methods were developed for the acquisition of 3D flow velocity maps and spatially resolved displacement propagators to study flow-structure correlations in a Ketton limestone rock at a pore-scale resolution.

Flow MRI is an integration of a pulsed field gradient nuclear magnetic resonance (PFG NMR) experiment [19], which is used to quantify fluid displacements, with an MRI experiment, which spatially resolves those displacements. Two different spatially resolved flow MRI measurement techniques can be distinguished. In the first case, a single, average velocity is spatially resolved for each of the voxels within an image—a method referred to as velocity mapping. In the second technique, a spatially resolved displacement propagator is acquired. Displacement propagators, otherwise known as van Hove self-correlation functions, are probability distributions of molecular displacements, $\bar{P}(\mathbf{R}, \Delta)$, where $\bar{P}$ is the probability that a spin moves over a dynamic displacement, $\mathbf{R} = \mathbf{r}' - \mathbf{r}$, in an observation time, Δ (typically in the range between a few ms up to the spin-lattice relaxation time, T_1, of the fluid, which may be up to a few seconds). By spatially resolving the displacement propagator, information about local, time-dependent flow dispersion, which arises due to molecular self-diffusion of fluid molecules across streamlines, can be obtained, as well as measurements of flow velocity.

X-ray μCT has also been used to study displacement processes in rocks [3,17,20]. Measurements are achieved by tracking the movement of a fluid interface between two different fluid phases. In contrast, flow MRI offers a direct and robust measurement of a flow velocity within a fluid phase and is a well-established tool for studying flow phenomena in porous media.

In this study, the NMR signal originates from ^{1}H spins within water molecules, and so the velocity maps and displacement propagators of water molecules are measured. Only single-phase flow MRI experiments will be shown, but two-phase (oil-water) sensitivity is straightforward to implement, without a need for doping of the fluids to enhance image contrast [6], and will be demonstrated in future work. The underlying principles of compressed sensing MRI and flow MRI have been described elsewhere [15,21–23] and will not be reviewed in detail here.

From the experimental perspective, velocity mapping and acquisition of a spatially resolved propagator are based on similar NMR experiments—data are acquired by combination of a displacement-encoding PFG NMR experiment to encode displacements, and an imaging experiment to acquire the image, though there are likely to be different requirements for the pulse sequence chosen. For example, velocity imaging experiments usually require a short observation time, Δ, such that there is no acceleration of the fluid over Δ and therefore an accurate instantaneous velocity can be calculated. In contrast, spatially resolved propagator measurements may use a range of larger Δ to investigate the effects of self-diffusion and fluid mixing over a longer timescale.

A schematic of the velocity-encoded MRI pulse sequence used to acquire velocity maps is shown in Fig. 1; it combines a pulsed gradient spin echo (PGSE) [19] sequence that is used to encode for velocities, with a rapid acquisition with relaxation enhancement (RARE) [24] imaging sequence that is used to spatially encode the measured velocities. The RARE sequence was selected, as it is well suited for CS applications and imaging fluid-saturated porous rocks, as is described in our earlier papers [14,18]. A PGSE sequence was selected for velocity encoding as Δ is short compared to signal decay rates in the transverse plane, and so signal loss was small compared to using a stimulated echo sequence which would inherently suffer from a 50% loss of signal [22]. Spin-echo-based PFG imaging sequences have successfully been used in the past to acquire accurate velocity maps in porous media [12,25,26]. Holland *et al.* [25] used a spin echo velocity imaging sequence, wherein each echo was acquired per
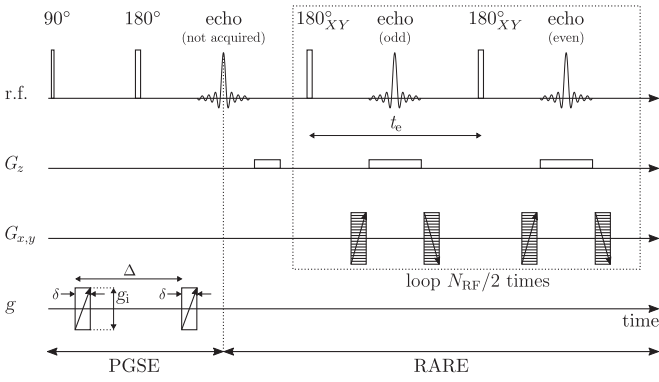
FIG. 1. Schematic of the pulse sequence used to acquire high-resolution velocity maps. It combines a pulsed gradient spin echo (PGSE) sequence with a rapid acquisition with relaxation enhancement (RARE) imaging sequence used for velocity and spatial encoding, respectively. The velocity encoding is achieved by a pair of unipolar gradients of strength g and duration δ, separated by an observation time, Δ. The spatial encoding is achieved using the frequency-encoding gradient, G_z, and the phase-encoding gradients, G_x and G_y. A RARE factor (N_{RF}) is the number of $180°$ refocusing pulses in an echo train. t_e is the echo spacing.

signal excitation, in combination with compressed sensing, to acquire quantitative two-dimensional (2D) velocity maps of liquid and gas flow through a packed bed of spherical glass beads at spatial resolutions of 178 and 230 μm, respectively. To speed up the acquisition of velocity maps, Huang *et al.* [12] combined a spin-echo-based velocity encoding module with a (fully sampled) RARE sequence to image water flow through porous deep bed filters at an isotropic spatial resolution of 160 μm. In this work, both the RARE sequence and a compressed sensing approach are exploited to speed up acquisition and enable 3D velocity mapping at 35 μm spatial resolution.

A schematic of the pulse sequence used to acquire spatially resolved propagators is shown in Fig. 2. This sequence has been described in detail in an earlier paper [13], where the acquisition of 3D spatially resolved propagators of flow in rocks was demonstrated at a much coarser spatial resolution than

is shown in this work. This sequence combines an alternating pulsed gradient stimulated echo (APGSTE) [27] sequence that is used to encode for displacements, with the RARE imaging sequence used in the velocity imaging sequence [28]. A stimulated echo sequence is needed for the longer observation times used for the propagator measurements. The APGSTE, or Cotts 13-interval, sequence has been selected as it has been shown to minimize the signal loss due to motion in background field gradients and is well suited to measurement of flow in porous media. Note that in general the measurement time of spatially resolved propagators is longer than that of velocity mapping because images need to be acquired for a range of **q**-space (i.e., the reciprocal space of dynamic displacements) points, whereas only two images at different **q**-space values are required to reconstruct a velocity map.

III. MATERIALS AND METHODS

A. Materials

A Ketton limestone rock core plug, 3.84 ± 0.01 mm in diameter and 11.10 ± 0.37 mm in length, was used in this study. After drying the sample in an oven at $70\,°$C for 12 h and acquiring μCT images, the rock sample was vacuum-saturated with deionized water; based on gravimetric analysis, the porosity (ϕ_g) of the rock sample was estimated to be $\phi_g = 21 \pm 4\%$. For the flow MRI experiments, the sample was placed in Adtech fluorinated ethylene propylene (FEP) heat shrink tubing which was used to connect the sample to inlet and outlet FEP tubing and to provide confinement. A constant flow rate of water was imposed using a Vindum VP-6 metering pump. Imposed flow rates were accurate to within 0.1% of the set point.

B. X-ray microcomputed tomography

The (dry) Ketton rock core plug was imaged using a Bruker SkyScan 1172 micro-CT scanner (Bruker Micro-CT, Belgium) at an isotropic resolution of 5.00 μm. Imaging was performed using a source voltage of 60 kV, a source current of 165 μA, and an Al (0.5 mm) filter. 802 projection images (10 scans per position) were acquired by rotating the
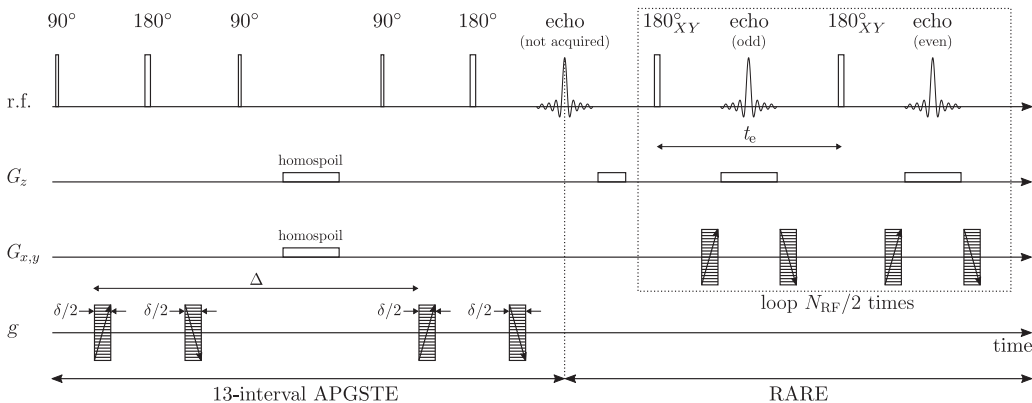
FIG. 2. Schematic of the APGSTE-RARE pulse sequence used to acquire 3D spatially resolved propagators. It consists of a 13-interval APGSTE sequence and a RARE imaging sequence. The displacement encoding was achieved by gradients g, which can be applied in any of the three orthogonal directions (z, x, or y). In this work, the displacement-encoding gradient was applied parallel to the superficial flow direction (z). The spatial encoding was achieved by the frequency-encoding gradient, G_z, and phase-encoding gradients, $G_{x,y}$.

sample through 200.5° with a 0.25° rotation step resulting in a total acquisition time of ~11.5 h. Projection images were reconstructed using the NRecon software (Bruker, v1.6.8.0) to give 2666 cross-sectional slices. A 3D μCT image of the rock sample was generated by successively stacking all 2D cross-sectional slices.

C. Magnetic resonance imaging experiments

Three pore-scale MRI data sets were acquired on the Ketton plug: a velocity map and two spatially resolved propagators, with different observation times (Δ), as detailed below. The experiments were carried out on a 7.0 T vertical-bore magnet controlled by a Bruker BioSpin Avance III HD spectrometer. A Bruker Micro5 tri-axial gradient system with a maximum gradient strength of 2.9 T m^{-1} in the three orthogonal x-, y-, and z-directions was used to achieve spatial resolution. An 8 mm radio frequency (r.f.) saddle coil tuned to a resonance frequency of 299.84 MHz (^{1}H) was used for spin excitation and signal detection.

A velocity map was also acquired for water flow through a packed bed comprising spherical 4-mm-diameter glass beads, with velocities encoded in the superficial flow direction (z); the internal diameter and the length of the bead pack were 38 mm and 69 mm, respectively. The experiment was conducted on a Bruker vertical super-wide bore superconducting magnet with a static magnetic field strength of 7.1 T (300.87 MHz ^{1}H resonance frequency) in combination with a Bruker Avance III spectrometer. An r.f. coil of diameter 66 mm was used, and the maximum magnetic gradient strength available was 0.78 T m^{-1}.

1. 3D velocity map acquisitions

A PGSE-RARE experiment (Fig. 1) was used to acquire undersampled velocity maps in Ketton rock. The duration of the hard 90° excitation and 180° refocusing r.f. pulses were 6 and 12 μs, respectively. Velocity encoding was achieved by a pair of unipolar gradients **g** of amplitude $g = 2.0$ T m^{-1} ($g_i = 4.0$ T m^{-1}) and duration of $\delta = 0.132$ ms either side of the first 180° pulse, separated by an observation time $\Delta = 4$ ms. Spatial encoding was attained by using a 3D RARE experiment, where the z-dimension (k_z) is frequency encoded and the x- (k_x) and y-dimensions (k_y) are phase encoded. The RARE factor (N_{RF}), which is the number of the echoes in an echo train per single excitation, was 8 with an echo spacing (t_e) of 2.2 ms. 32 scans were acquired for signal averaging with a recycle delay (t_{RD}) of 1.1 s and a **k**-space sampling fraction of 0.25, giving a total acquisition time of 20 h for a single velocity component (i.e., for a velocity map with velocities encoded in one direction). To correct for the velocity offsets caused by gradient imperfections, no-flow images (images acquired with the pump switched off) were also acquired for each image. The images were acquired with a field of view (FOV) of 13.5 mm×4.5 mm×4.5 mm and 384 voxels×128 voxels×128 voxels in the z-, x-, and y-directions respectively, yielding 3D images with an isotropic resolution of 35.2 μm. During image acquisitions, a constant flow rate of water of 0.03 ml min^{-1} was imposed, which corresponds to an interstitial flow velocity (v_i) of 91 ± 3 ft day^{-1}, where the estimate of v_i is based on the macroporosity of the Ketton

sample between 13% and 14%. Note that if we assume the characteristic length of this system, l_c, to be equal to the typical grain diameter of approximately 0.5 mm, the Reynolds number, Re $= \frac{l_c v_i}{\nu_f}$, where ν_f is the kinematic viscosity of fluid, is Re $= 0.16$. Given that Re $\ll 1$, the flow is in the Stokes regime at the given flow rate.

Sampling patterns for the acquisition of velocity maps were generated using the μCT-based variable density sampling (μCT-VDS) strategy described in our previous work [8]. In the current work, the method was used to generate optimized **k**-space sampling patterns with a **k**-space sampling fraction of 0.25. The **k**-space sampling fraction of 0.25 was chosen as it was found to give a good balance between the reduction of image acquisition time and the quality of reconstructed images. The order in which **k**-space points from the optimized sampling scheme were sampled experimentally was determined using an approach described in our previous work [14]. This approach sorts **k**-space sampling trajectories in the echo train in such way that ensures uniform relaxation weighting across **k**-space.

The velocity map of the packed bed was acquired using a fully sampled (no undersampling) PGSE-RARE experiment. The duration of the hard 90° excitation and 180° refocusing r.f. pulses were 78 μs and 156 μs, respectively. The flow imaging parameters were $g = 0.5$ T m^{-1} ($g_i = 1.0$ T m^{-1}), $\delta = 0.586$ ms, and $\Delta = 6$ ms. 4 scans were acquired with $N_{RF} = 32$, $t_e = 2.1$ ms, and $t_{RD} = 0.6$ s, yielding an experimental time of 41 min for a single velocity component. To correct for the velocity offsets, a no-flow image was also acquired. The FOV was set to 8.00 cm × 4.00 cm × 4.00 cm with 256 voxels×128 voxels×128 voxels in the z-, x-, and y-directions, respectively, giving a 3D image with an isotropic resolution of 312.5 μm. During flow imaging experiments, a constant flow rate of water of 9.5 ± 0.5 ml min^{-1} was imposed using a Cole-Parmer Masterflex® peristaltic pump. The estimated interstitial flow velocity was $v_i = 94 \pm 5$ ft day^{-1}.

2. 3D spatially resolved propagator measurements

For the acquisition of the spatially resolved propagators, an APGSTE-RARE experiment (Fig. 2) was used with the following parameter settings. The duration of the hard 90° excitation and 180° refocusing r.f. pulses were 6 μs and 12 μs, respectively. The number of echoes acquired in each echo train was $N_{RF} = 8$ with $t_e = 4.2$ ms.

Two different spatially resolved propagators were acquired with different observation times Δ, namely, $\Delta = 150$ ms and $\Delta = 900$ ms. Between the two experiments, the imposed interstitial flow velocity v_i was scaled as the inverse of observation time, so that the total interstitial displacement $v_i \Delta$ is identical between the two experiments and the effects of self-diffusion can be observed. For the observation time of 150 ms, a fluid flow rate of 0.03 ml min^{-1} ($v_i = 91 \pm 3$ ft day^{-1}) was imposed, hence the experiment with an observation time of 900 ms was performed at a flow rate of 0.005 ml min^{-1} ($v_i = 15 \pm 1$ ft day^{-1}).

Displacement encoding was achieved using two pairs of bipolar gradients **g** of duration of $\delta/2 = 0.14$ ms and maximum amplitude of $g = 2.8$ T m^{-1} for $\Delta = 150$ ms and $g = 1.3$ T m^{-1} for $\Delta = 900$ ms.

The 3D spatially resolved propagators were acquired with a FOV of 13.5 mm×4.5 mm×4.5 mm and 144 voxels×48 voxels×48 voxels in the frequency- (z) and both phase-encoding directions (x and y), respectively, yielding 3D images with an isotropic resolution of 93.8 μm. In **q**-space, 65 points were acquired, leading to a FOV in the displacement direction of 1.0 mm. The displacement direction was chosen to be parallel to the superficial flow direction (z).

The following method was used to generate an under-sampling pattern for the 3D spatially resolved propagators, which is a further development of the approach described in Ref. [13]. For a 3D spatially resolved propagator experiment, a 3D **q**-**k**$_{\text{phase}}$-space undersampling pattern is required. Thus, the shape of the probability density function (pdf) describing the undersampling pattern is generated based on (1) the μCT-VDS approach for 2D **k**$_{\text{phase}}$-space and (2) the shape of one-dimensional **q**-space derived from a spatially unresolved propagator experiment, which is quick to acquire. The two pdfs are multiplied to obtain a 3D probability distribution function, on the basis of which a sampling pattern was generated at a sampling fraction of 0.25.

Using $t_{\text{RD}} = 2$ s, and acquiring 16 signal averages at a sampling fraction of 0.25 of **k**,**q**-space, the acquisition time of the spatially resolved propagators was 4 days for the $\Delta = 150$ ms experiment and 5 days for the $\Delta = 900$ ms experiment—this is 32 times faster than a fully sampled, simple spin echo MRI experiment at the given signal-to-noise ratio (SNR). The sample remained in the same position for both the velocity map and spatially resolved propagator experiments.

D. Image processing

1. Compressed sensing reconstructions of undersampled flow data

CS reconstructions of undersampled MRI flow data follow a similar approach as used in earlier work [21]. In flow imaging, the goal is to recover the phase of a complex-valued image, **m**, from an acquired undersampled **k**-space data set, **y**. CS enables us to find a solution for **m**, **m**$_{\text{CS}}$, using a variational regularization approach which incorporates prior knowledge about **m** into the reconstruction process. In the case of CS MRI, the prior knowledge is that the image can be sparsely represented in an appropriate transform domain. The type of regularization functional J that is used to map the image into the transform domain depends on the nature of the image to be mapped. In this work, total variation (TV) regularization, which is based on the finite-difference transform of **m**, was used as we have already demonstrated that TV yields a good reconstruction quality for velocity maps [21,25] and spatially resolved propagators [13,18]. Finally, using a nonlinear recovery algorithm, a solution for **m**$_{\text{CS}}$ is computed on the basis of this prior knowledge, expressed as

$$\mathbf{m}_{\text{CS}} \in \arg\min_{\mathbf{m}} \left[\frac{1}{2} \|\mathbf{y} - \mathcal{F}_u \mathbf{m}\|_2^2 + \alpha J(\mathbf{m}) \right], \qquad (1)$$

where α is a regularization parameter that balances the weight between the fidelity term $\frac{1}{2}\|\mathbf{y} - \mathcal{F}_u \mathbf{m}\|_2^2$ and the regularization term $\alpha J(\mathbf{m})$. The value of the parameter α was chosen on the basis of Morozov's discrepancy principle [29], which is

written as

$$\|\mathbf{y} - \mathcal{F}_u \mathbf{m}\|_2 \leqslant \sigma_n \sqrt{n}, \qquad (2)$$

where n is the number of **k**-space samples. The maximum value of α which satisfies the condition in Eq. 2 was chosen for the reconstructions. The CS reconstructions were carried out using an in-house Matlab toolbox, Object Oriented Mathematics for Inverse Problems, for which the implementation was reported in Ref. [21].

2. Generating velocity maps

First, the individual undersampled **k**-space data sets under flow and no-flow conditions were reconstructed separately to yield complex-valued MRI images. The velocity maps were then calculated from these phase maps using standard procedures. It is noted that phase maps were calculated for the odd and even echoes separately, and the resulting phase difference maps of odd and even echoes were recombined by voxel-wise averaging for improved accuracy [12] of the velocity maps. The magnitude images of the no-flow MRI data sets were then averaged to generate a binary mask which was multiplied by the velocity maps to null the background noise in the velocity maps. The magnitude image was binarized using the watershed-based segmentation algorithm [30] in Avizo 2019.4 (FEI Visualisation Sciences Group, USA). The velocity maps were processed in Matlab (Mathworks, USA).

It is noted that the watershed-based segmentation algorithm was chosen for image binarization as it can effectively deal with partial volume effects (due to voxels located at the pore-grain interfaces). Inevitably, some voxels in the final masked velocity image will still contain both fluid and rock matrix phases. However, the flow data will not be intrinsically adversely affected, unless the SNR becomes too low, which can happen if only a very small part of the voxel contains fluid. In this work, the flow measurements were shown to be accurate overall, as there was excellent agreement between the imposed flow velocities and velocities estimated from flow data (see Sec. IV).

3. Structure-transport correlations of velocity maps

To obtain structure-transport correlations in the Ketton rock, the binarized magnitude (structural) image and the velocity map of flow through the rock acquired in the superficial flow direction (z) were analyzed in Avizo. The pore space of the binarized structural image was separated into individual pores using a Chamfer distance transform and marker-based watershed algorithm. The structural image and the velocity map were used to correlate the flow properties for the individual pores. Equivalent effective pore body radii (i.e., the radius of a sphere with the same volume as a pore) and coordination numbers of the labelled pores were obtained using the "Generate Pore Network Model" module [31].

4. Image coregistration

Image coregistration of the MRI and μCT data sets was performed in Avizo using the "Register Images" module. The alignment of the μCT image relative to the reference image (i.e., the magnitude image of the acquired MR data) was optimized using an automatic image registration based

on rigid transformations and normalized mutual information [32,33]. The optimization procedure was performed in steps at different spatial resolutions for more time-efficient coregistration. During the coarsest-resolution optimization, MRI and μCT data were down-sampled by a factor of 2 and 14, respectively. Extensive Direction and Quasi Newton optimizers were used for the coarse resolution and the finest resolution images, respectively [34]. Once the registration process was completed, the coregistered μCT data set was resampled onto the MRI data coordinate system using a Lanczos filter [35]. This allowed for the MRI flow maps and μCT images to be compared on the same grid. For the coregistration of the spatially resolved propagator, a higher-resolution MRI image of the rock acquired with the exact same sample position was used as a reference image. The resampled μCT image and MRI data were then visualized as a combined (fused) data set.

IV. RESULTS AND DISCUSSION

This section is structured as follows. First, in Sec. IV A, the pore-scale resolution 3D velocity map of flow through the Ketton plug is presented. It is then described how the map is coregistered and fused with a high-resolution μCT image of the same rock sample and visualized as a single data set to correlate structure and flow information. In Sec. IV B, it is shown how a 3D spatially resolved propagator acquired for flow through the Ketton plug is segmented into the representative flowing and stagnant components and then fused with an aligned μCT image. The effects of using different observation times on the shape of a spatially resolved propagator are also discussed.

A. Velocity map

1. Characterization of 3D MRI flow fields in Ketton rock

Figure 3(a) shows the magnitude map of the combined z-, x-, and y-velocity components for flow of water in Ketton rock at the imposed flow velocity of $v_i = 91 \pm 3$ ft day^{-1} (0.32 ± 0.01 mm s^{-1}). By visually inspecting the flow map, two characteristics are observed. First, it is seen that most water in the pore space of Ketton rock has low mobility, with a typical speed < 0.2 mm s^{-1}. Nearly 70% of the voxels in this region of the rock contain fluid flow with lower speed than the mean absolute flow speed of approximately 0.5 mm s^{-1}. Second, the flow is heterogeneous and is concentrated in a few high-velocity flow channels. These observations are consistent with the results obtained from flow MRI measurements in glass bead packs [36,37] and micron-scale flow simulations in carbonate rocks [38]. They are also consistent with the notion that the conductance of a pore scales as the pore radius to the power of four, which, in a porous medium with a distribution of pore sizes, leads to the flow being concentrated in a number of critical paths which carry most of the flow [39,40]. The velocity distributions of v_z and v_y components are shown in Fig. 3(b) and Fig. 3(c); the velocity distribution of the v_x component is not shown but is similar to the distribution of the v_y component. The distribution of v_z exhibits a long positive tail, a significant intensity at $v_z = 0$ mm s^{-1} which represents stagnant water, and some negative flow or backflow, represented by negative velocities. The long positive

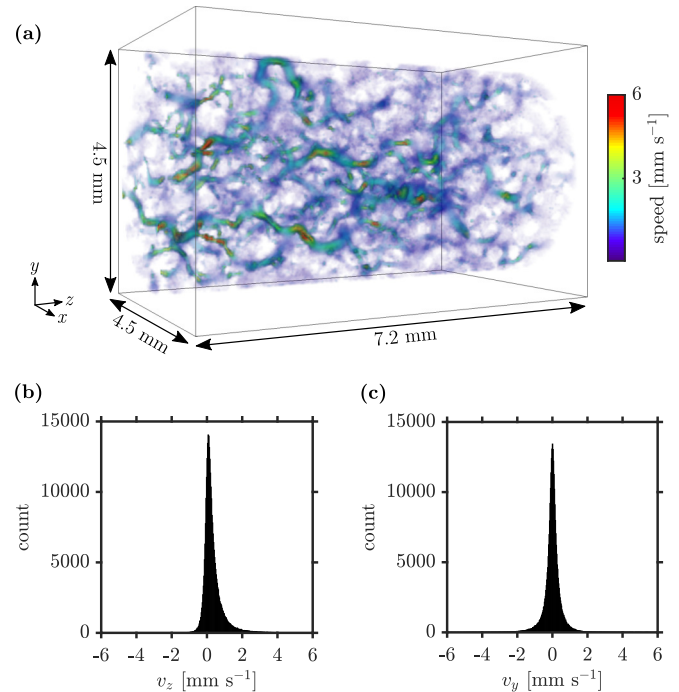FIG. 3. (a) Pore-scale 3D magnitude flow map generated from the x-, y-, and z-velocity components showing the main flow channels through the Ketton rock plug. Velocity distributions of (b) z- and (c) y-velocity components; the x-velocity component has a similar distribution of velocities to the y-velocity component.

tail illustrates the heterogeneity in the flow through Ketton rock with the highest velocities extending to $\sim$50 times the modal velocity of $v_z \sim 0.08$ mm s^{-1}. The mean velocity along the superficial flow direction (z) was calculated to be $v_z = 0.32$ mm s^{-1} (91 ft day^{-1}), which is in excellent agreement with the imposed interstitial flow velocity in the macropores. The occurrence of backflow in flow through porous media has been identified both in flow computations [41,42] and physical (MRI) flow experiments [26,43–45] and is believed to be caused by recirculating flow patterns in the immediate vicinity of surfaces, or vortex-like structures at the meeting points of streamlines. Backflow has been observed in experimental studies of flow through a variety of bead packs with different bead geometries and sizes [43,44] and at various flow rates (Re > 1) [43]. It has also been predicted using lattice Boltzmann method simulations in a bead pack for a range of Re = 0.6 − 30 [42] that the degree of backflow is dependent on Re and increases with Re. In this work, the backflow phenomenon is present even at a relatively low Re of 0.16, i.e., during Stokes flow. This is perhaps not entirely surprising, since Saeger *et al.* [41] demonstrated, by solving the Navier-Stokes equation, that recirculating flow patterns are identified for Stokes flow in bicontinuous porous media. The distribution of v_y is symmetric around $v_y = 0$ mm s^{-1} (i.e., zero net flow) with velocities up to $v_y \sim \pm 2$ mm s^{-1}. It was found that the positive and negative parts of the distribution of v_y are described well by a single-exponential function, which is consistent with findings elsewhere [46].

To analyze in more detail how the flow is distributed across the pore space of Ketton rock, structure-transport information
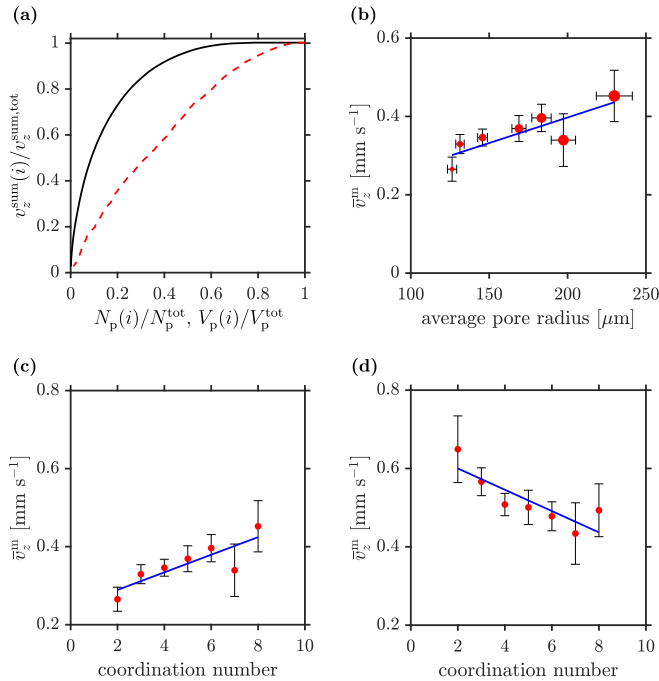
FIG. 4. Structure-flow correlations in Ketton rock. (a) The fractional summed z-velocities (in the superficial flow direction) within pores with a summed z-velocity equal to or greater than (the parametric variable) i, $v_z^{\mathrm{sum}}(i)/v_z^{\mathrm{sum,tot}}$, plotted as a function of the fraction of the number of pores, $N_{\mathrm{p}}(i)/N_{\mathrm{p}}^{\mathrm{tot}}$ (–), and the volume of pores, $V_{\mathrm{p}}(i)/V_{\mathrm{p}}^{\mathrm{tot}}$ (- - -), carrying this flow. (b) The average mean z-velocities, $\bar{v}_z^{\mathrm{m}}$, within pores plotted as a function of the average radius of these pores for different coordination numbers; the size of the red dots represents coordination numbers from 2 to 8 in ascending order. (c) Correlation between the average mean pore velocities, $\bar{v}_z^{\mathrm{m}}$, and coordination numbers for all pores. (d) Correlation between the average mean pore velocities, $\bar{v}_z^{\mathrm{m}}$, and coordination numbers for pores with local Reynolds numbers greater than the mean local Reynolds number of 0.064. The solid blue lines represent the regression fits to the data.

was extracted from the velocity component acquired in the direction of superficial flow (z) and from the pore-segmented structural image; the analysis was performed on the 3D region of the image of size 7.2 mm×4.5 mm×4.5 mm shown in Fig. 3(a). Figure 4 summarizes aspects of the structure-flow relationships extracted from the z-velocity component of the image shown in Fig. 3(a). Figure 4(a) shows the fraction of the total flow [$v_z^{\mathrm{sum}}(i)/v_z^{\mathrm{sum,tot}}$] as a function of the fraction of the number [$N_{\mathrm{p}}(i)/N_{\mathrm{p}}^{\mathrm{tot}}$] and volume [$V_{\mathrm{p}}(i)/V_{\mathrm{p}}^{\mathrm{tot}}$] of those pores that carry this flow. It is seen that more than half of the flow (∼53%) is carried by just 10% of the pores which represent approximately 36% of the pore volume in the rock. This analysis is consistent with the flow map in Fig. 3(a), in which it is seen that only a few flow channels carry a large proportion of flow through the rock. Fig. 4(b) shows the mean z-velocities within pores (v_z^{m}) averaged over pores with the same coordination number, i.e., the average mean velocity within a pore, $\bar{v}_z^{\mathrm{m}}$, plotted as a function of the average radius of these pores for different coordination numbers ranging from 2 to 8; the size of the red dots represents co-

ordination numbers from 2 to 8 in ascending order (i.e., the smallest dot represents pores with coordination number = 2). First, it is seen that the average pore size (as characterized by average pore radius) increases with the coordination number of the pore. A similar positive correlation between the pore size and coordination number in porous sandstone rocks has been reported elsewhere [47], which is expected because larger pores are more likely to have more throats feeding in to them. Second, larger pores tend to have greater values of mean pore velocity, v_z^{m}. Performing coordination number-independent analysis of the data, it was estimated that the average ± standard error (standard deviation) of v_z^{m} of the pores with pore radii smaller and greater than the mean pore radius of 120 μm are $0.25 \pm 0.02\,(0.40)\,\mathrm{mm\,s^{-1}}$ and $0.31 \pm 0.01\,(0.25)\,\mathrm{mm\,s^{-1}}$. Figures 4(c) and 4(d) consider the flow through the pores as a function of their coordination number. In Fig. 4(c) data for all pores with coordination numbers 2–8 are shown. The trend in the data suggests that mean flow velocity through a pore increases with the coordination number of the pore with average mean z-velocities within the pores increasing from $0.27 \pm 0.03\,\mathrm{mm\,s^{-1}}$ for a pore coordination of 2, up to $0.45 \pm 0.07\,\mathrm{mm\,s^{-1}}$ for a pore coordination number of 8. In Fig. 4(d) only the data for pores in which the local Reynolds number ($\mathrm{Re_l}$) is greater than the mean local Re are shown, where the local Re is defined as $\mathrm{Re_l} = \frac{A^{1/2}\bar{v}_z^{\mathrm{m}}}{v_{\mathrm{f}}}$ [36], where A is the cross-sectional area of a pore calculated from its radius, and v_{f} is the kinematic viscosity. It was estimated that the $\mathrm{Re_l}$ in the Ketton rock at $v_{\mathrm{i}} = 91\,\mathrm{ft\,day^{-1}}$ ($0.32\,\mathrm{mm\,s^{-1}}$) are all smaller than 1, therefore all the pores locally exhibit Stokes flow behavior. Within the Stokes regime, the flow field scales with global flow rate, and so to separate out those pores which carry most of the flow, it is justified to use the mean $\mathrm{Re_l}$ as a cutoff value—the result of the following analysis will not change with global flow rate. The mean $\mathrm{Re_l}$ is 0.064; approximately 36% of the pores (by number) are considered in this analysis. The mean flow velocity through a pore is now seen to decrease with increase in coordination number. Figures 4(c) and 4(d) are worthy of further inspection. It is seen that at the higher coordination numbers the pores have similar values of mean pore velocity. In contrast, at low pore coordination number—and, in particular, coordination of 2—pores carrying flow greater than the mean $\mathrm{Re_l}$ are associated with flow velocities more than double those seen in Fig. 4(c); i.e., $0.65\,\mathrm{mm\,s^{-1}}$ compared to $0.27\,\mathrm{mm\,s^{-1}}$. This observation is consistent with some of the pores identified as having a coordination number of 2 effectively being narrow constructions between high-volume pores which are carrying the majority of the flow through the bed. Indeed, interrogation of the image shown in Fig. 3(a) shows that some of the small regions associated with highest fluid velocities (indicated by red voxels) are correlated with the pores with low coordination number and a higher-than-average $\mathrm{Re_l}$.

Figure 5 shows the equivalent data recorded for a packing of 4-mm-diameter glass spheres. Qualitatively the trends remain the same as those shown in Fig. 4, suggesting that there are similarities in the flow behavior between a sphere pack and Ketton rock, the microstructure of which does indeed approximate a packing of spherical grains as is seen
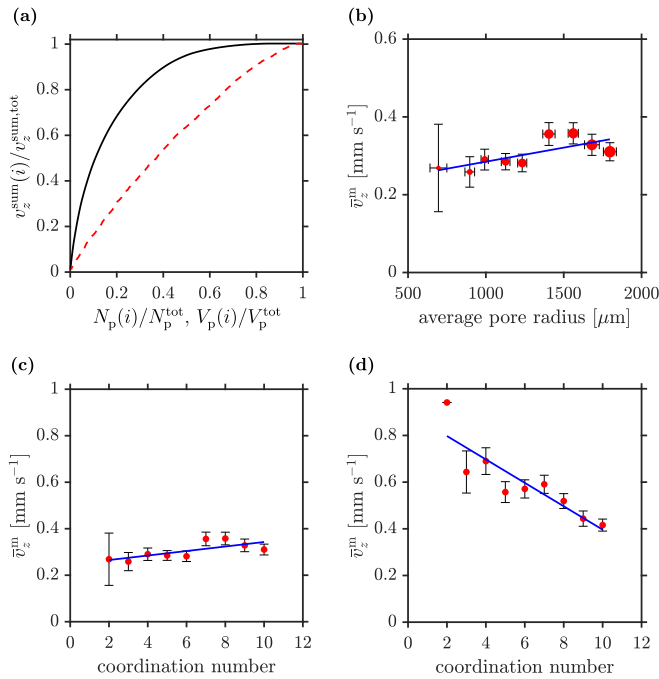
FIG. 5. Structure-flow correlations in a pack of spherical beads. (a) The fractional summed z-velocities (in the superficial flow direction) within pores with a summed z-velocity equal to or greater than (the parametric variable) i, $v_z^{\mathrm{sum}}(i)/v_z^{\mathrm{sum,tot}}$, plotted as a function of the fraction of the number of pores, $N_p(i)/N_p^{\mathrm{tot}}$ (−), and the volume of pores, $V_p(i)/V_p^{\mathrm{tot}}$ (- - -), carrying this flow. (b) The average mean z-velocities, $\bar{v}_z^{\mathrm{m}}$, within pores plotted as a function of the average radius of these pores for different coordination numbers; the size of the red dots represents coordination numbers from 2 to 10 in ascending order. (c) Correlation between the average mean pore velocities, $\bar{v}_z^{\mathrm{m}}$, and coordination numbers for all pores. (d) Correlation between the average mean pore velocities, $\bar{v}_z^{\mathrm{m}}$, and coordination numbers for pores with local Reynolds numbers greater than the mean local Reynolds number of 0.82. The solid blue lines represent the regression fits to the data.

in Fig. 6, although it has a lower porosity than the sphere pack. Figure 5(a) shows a similar shape to Fig. 4(a) and shows that 48% of the flow is carried by 10% of the pores which represent approximately 35% of the pore volume in the sphere pack. The data in Figs. 4(a) and 5(a) are also consistent with data reported earlier for 2D imaging of structure-flow relationships [36] in a packing of 5-mm-diameter spheres in which it was observed that 10% of the pores carried ∼42% of the flow. Similar to the correlations seen for Ketton rock in Figs. 4(b) and 4(c), Figs. 5(b) and 5(c) show that the mean pore velocity increases with increasing pore radius and coordination number for all pores with coordination numbers 2–8, although the dependency between these quantities appears to be slightly weaker for the bead pack in terms of the slope of the regression fit; for the bead pack data in Fig. 5(c), average mean z-velocities within the pores increase from 0.27 to 0.36 mm s^{-1} for coordination numbers 2–8 (vs 0.27–0.45 mm s^{-1} for the same range in coordination numbers in Ketton rock). Figure 5(d) shows that the mean flow z-velocity through a pore decreases with increasing pore coordination number for pores with Re$_l$ greater than the mean
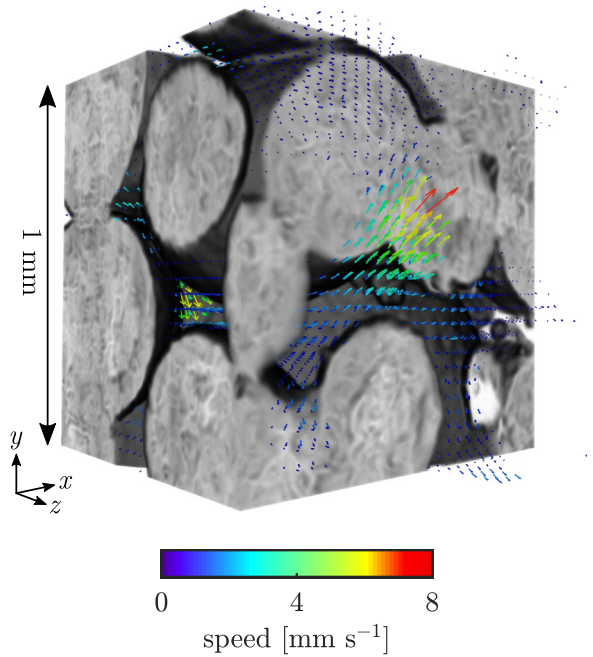

FIG. 6. A 3D section of 1 mm^3 extracted from the coregistered 3D MRI velocity vector map and μCT image of Ketton rock. The displayed 3D velocity vectors were obtained by combining z-, x-, and y-velocity components; arrows represent the direction of flow, and the size and color of these arrows represent the magnitude of the flow. The superficial flow direction was along the z-axis.

Re$_l$ of 0.82; a correlation which is again consistent with the Ketton rock data [Fig. 4(d)].

2. Coregistration of high-resolution MRI velocity maps and μCT images of Ketton rock

Figure 6 shows a 3D visualization of the combined z-, x-, and y-velocity components coregistered with the 3D μCT image. The magnitude and color of the arrows represent the speed of the fluid flow, and the direction of the arrows indicate the direction of the fluid flow through the rock. It can be seen in Fig. 6 that the speed of flow is higher up-stream and down-stream from the large ooid in the center of this rock section and that the high-velocity pore down-stream from this ooid has a high coordination number and is associated with high fluid velocity, consistent with the analysis shown in Fig. 4(c). In Fig. 7, 2D xy-slice images and 3D sections obtained from the 3D coregistered MRI and μCT data set are shown; the 2D velocity maps represent fluid flow velocities acquired in the superficial flow direction (z), while the 3D velocity maps represent all three orthogonal velocity components. The high spatial resolution of the coregistered data set enables us to identify different flow patterns in the rock and to correlate these patterns with the microstructure of the rock matrix. For example, in region 1 [Fig. 7(a)] complex flow behavior can be observed in a large pore where backflow, which is characterized by negative velocities along the superficial flow direction, has developed adjacent to relatively high-velocity forward-flow channels. A 3D visualization of this region is shown in Fig. 7(c). It can be seen that the backflow occurs because the flow in the z-direction is obstructed and diverted
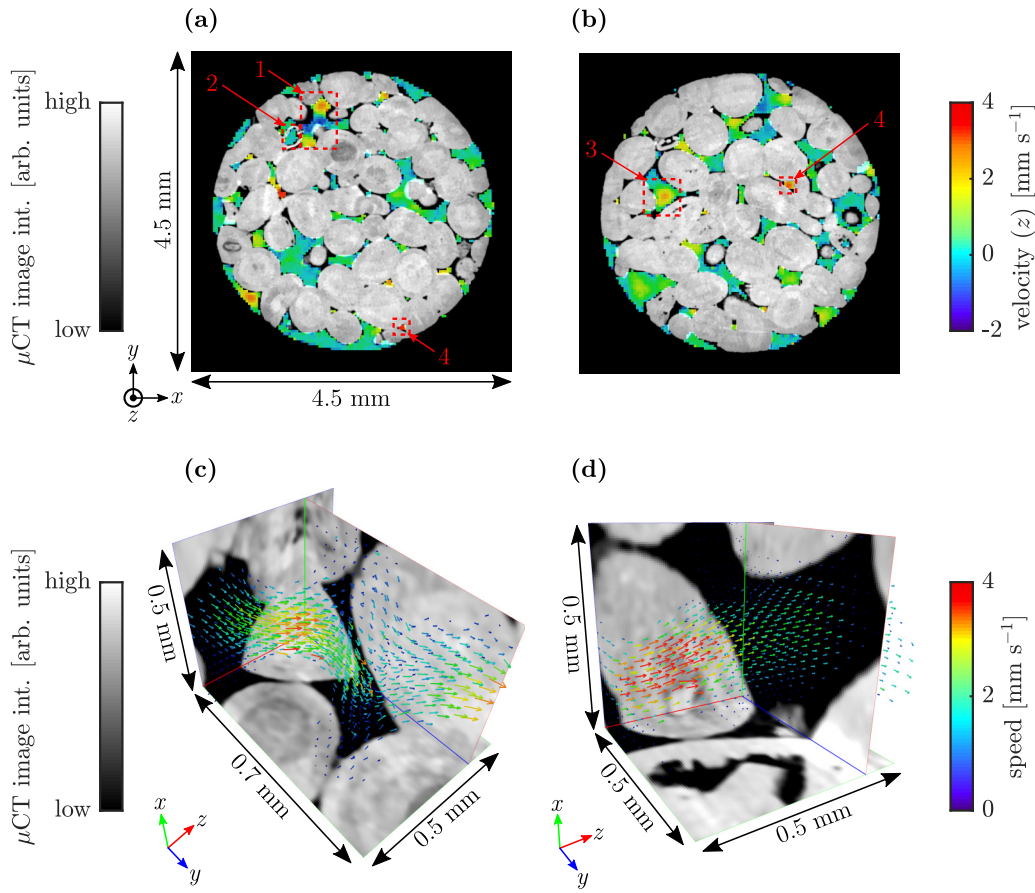
FIG. 7. (a), (b) 2D xy-slice images extracted from a 3D coregistered z-velocity map and μCT image of Ketton rock. Four regions have been highlighted by the red boxes which identify different flow patterns in the the rock: (1) adjacent positive and negative flow in a large pore; (2) stagnant water in a moldic pore; (3) high-velocity flow channel in a large pore; and (4) concentrated flow in the narrow parts of pores. Regions (c) 1 and (d) 3 are also visualized as coregistered 3D velocity (x, y, z) vector maps.

by the rock grains. In region 2, a moldic pore can be seen, in which water appears to be stagnant; moldic pores are carbonate-specific microstructural features, developed by the dissolution of a preexisting constituent of a rock, such as a shell or grain. It was verified that this moldic pore has very restricted and narrow openings. In Fig. 7(b) region 3, a wide, high-velocity flow channel can be seen in a macropore, which is also illustrated in Fig. 7(d) in the 3D velocity vector map. In the 2D velocity maps shown in Fig. 7, it can be seen that the flow velocity of fluid becomes increasingly high when it passes through narrow pore spaces formed by the tightly packed Ketton ooids, some of which are labeled as region 4.

B. Spatially resolved propagators

The 3D spatially resolved propagator data are four-dimensional: they contain three spatial dimensions and a displacement dimension. Such data are therefore amenable to two different types of analysis. The first type of analysis is image-based and is related to the fact that for each of the displacement points on the propagator, a 3D intensity image exists which shows where the fluid is located which has displaced over that particular distance during the observation time, Δ. The second type of analysis is propagator-based and is related to the fact that in each of the voxels in the spatially

resolved propagator, a local propagator can be found, which contains information about the distribution of displacements that the fluid molecules in that location have undergone during the observation time, Δ. Some of the molecules that are located within a particular voxel after Δ has elapsed, may have started in another voxel and moved into the voxel of interest during Δ. Because both the duration of the observation time and the flow rate can be chosen freely, this effect will be stronger for higher flow rates and longer observation times; in such cases, the propagator contains information about flow processes upstream of that particular voxel.

Furthermore, the data were used to explore whether or not the sample studied was sufficiently large to constitute a representative elementary volume (REV), which was based directly on the flow properties of the rock. To do this, the shape of the local propagator was compared to that of the global propagator across different length scales by spatially averaging the local propagators between adjacent voxels.

An example of an image-based analysis is shown in Fig. 8. The spatially resolved propagator was used to segment the pore space into stagnant and flow-carrying components. The global, nonspatially resolved propagator, obtained by summation of all 331 776 individual, per-voxel propagators, is shown in Fig. 8(a). The flow observation time, Δ, was 150 ms, at an interstitial flow velocity of 91 ft day^{-1}. The global
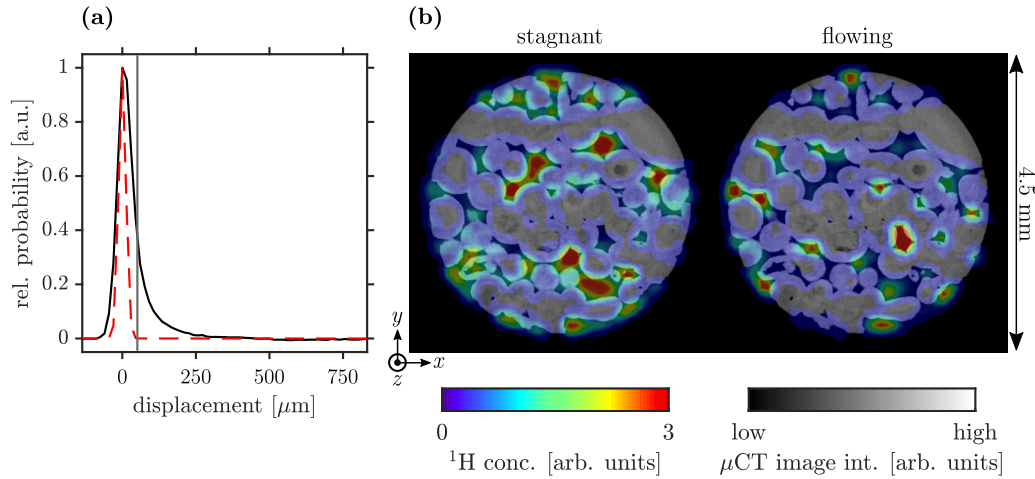
FIG. 8. (a) Global propagator, obtained by summation of all 331 776 individual, per-voxel propagators (–) and the expected Gaussian propagator (– – –) for water in the absence of flow. The gray, vertical line represents a cutoff between the "flowing" and "stagnant" water. Based on this cutoff, the (b) stagnant and flowing water images were generated and coregistered with the high-resolution μCT image of Ketton rock. The displayed colors in (b) represent the average of colormaps of MRI and μCT images.

propagator shows that a significant amount of fluid is stagnant or near-stagnant, whilst a much smaller amount of fluid is significantly displaced during Δ. A cutoff between "flowing" and "stagnant" water, which is indicated by the gray vertical line in Fig. 8(a), was chosen based on the expected Gaussian shape of the propagator for water molecules in the absence of flow (the self-diffusion coefficient, D, is 2×10^{-9} m^2 s^{-1} at room temperature). The cutoff was applied at the right-hand tail of the distribution; due to self-diffusion alone (i.e., under no-flow conditions), the molecules would have less than 1% chance of displacing beyond the cutoff. The stagnant and flowing water was then spatially resolved, as shown in the two complementary images in Fig. 8(b). The data were coregistered and fused with a μCT image of the same rock. In contrast to the coregistered images in Fig. 7, the colormap in Fig. 8(b) indicates the *amount* of fluid in each voxel which is either stagnant or flowing, whereas Fig. 7 represents the average velocities of fluid flow through rock. Overall, the trends seen in Fig. 8(b) are consistent with those observed in velocity maps—the proportion of the fluid that has a significant displacement that can be attributed only to the imposed flow is carried by a small fraction of the pore space. This simple workflow can therefore be used to obtain an estimate of the fraction and spatial distribution of the flow-carrying porosity. Because the spatial and displacement resolutions in a spatially resolved propagator can be chosen independently, this approach can also be used with larger rock core samples at coarser spatial resolutions in order to identify flow-carrying porosity, which will be a topic of future work.

In Fig. 9, a propagator-based perspective is taken on the data. In this case, the effect of observation time, Δ, on the shape of individual, per-voxel propagators is investigated. The results of two separate experiments are shown—recall that between the two, the product of observation time and interstitial flow velocity was kept constant, such that the global mean fluid displacement within the rock during observation time Δ is identical. The idea behind this approach is that this gives insight into the extent of diffusive coupling between

stagnant and flowing zones on the length scale of a single voxel, rather than on the global level, as was the subject of earlier work [48]; because the mean displacement is the same between the two experiments, the flow dispersion in the absence of self-diffusion would be identical, assuming that the streamlines are identical between the two cases.

Figure 9(a) shows two spatially unresolved (global) propagators normalized to the same area, which are the sum of the 331 776 local propagators in each of the two data sets. The mean displacement in both propagators, which should be identical, is 45 ± 5 μm for the $\Delta = 150$ ms and 39 ± 5 μm for the $\Delta = 900$ ms data set—this corresponds to interstitial flow velocities of 85 ± 9 and 12 ± 2 ft day^{-1}, respectively (to be compared with the imposed flow velocities of 91 ± 3 and 15 ± 1 ft day^{-1}). The measurement is therefore quantitative to within the error margin, with the slightly larger percentage deviation from the expected flow velocity for the $\Delta = 900$ ms experiment probably due a lower SNR for that experiment, because of the longer observation time Δ. It is seen that although the mean displacement between the two experiments is the same, the propagator of the $\Delta = 900$ ms experiment is much broader due to additional self-diffusion and flow dispersion relative to the $\Delta = 150$ ms experiment. This can be seen also from the Péclet numbers, Pe = Re $\frac{v_f}{D}$, which equal 80 for the higher flow rate and 13 for the lower flow rate. These numbers confirm that the fluid transport through the rock is significantly less dominated by advective transport at the lower flowrate. In both cases, the propagators are positively skewed, which is typically seen in the regime where the mean displacement is significantly smaller than the characteristic length (grain size) within the porous medium, so that the propagators are still close to being a projection of the distribution of short-time velocities [49]. Only at long timescales will the propagator transition back to a fully dispersive, Gaussian shape, as has been shown in various studies by different groups [38,48–57].

The spatially resolved approach shown in this work allows zooming into the regions where most of the flow and
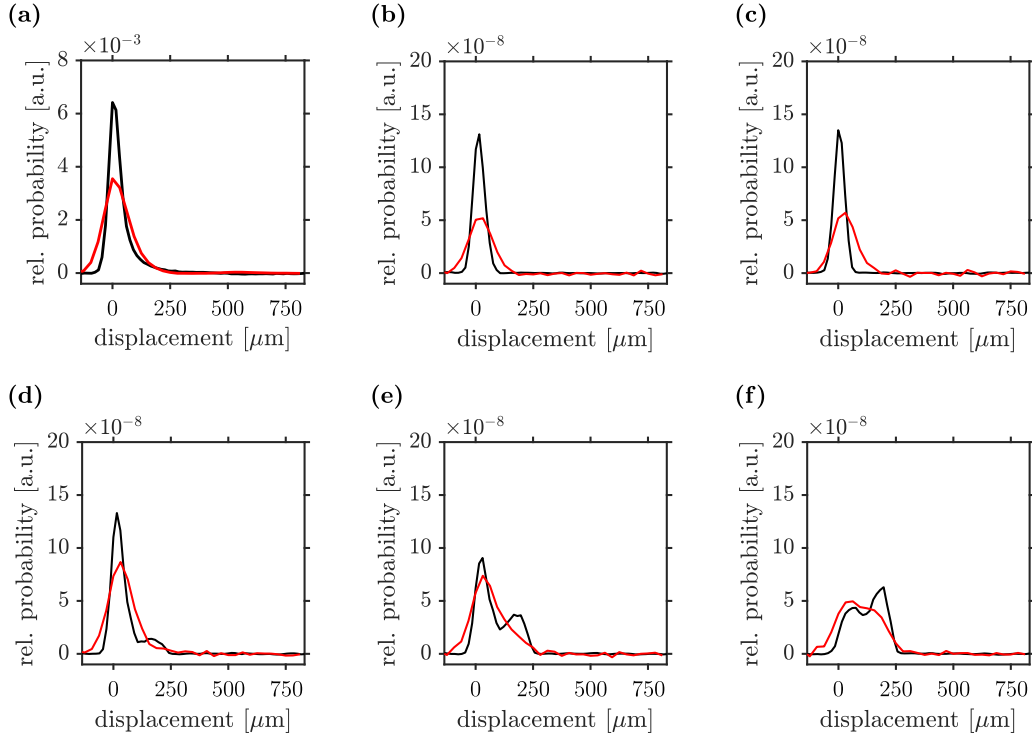
FIG. 9. (a) Global propagators, obtained by summation of all 331 776 local propagators of the $\Delta = 150$ ms (**–**) and 900 ms (——) data sets. (b–f) Five examples of local, per-voxel propagators, plotted on the same scale as the propagators in (a).

therefore flow dispersion occurs. In these regions, significant flow dispersion is observed which is not readily seen in the global propagator. Figures 9(b)–9(f) show five examples of local propagators taken from the 3D data set; note that the displacement axis of the propagators is broader (1 mm) than the underlying voxel resolution (94 μm), so that the starting positions of the fluid molecules in each voxel may lie outside of a particular voxel. A comparison is again made between local propagators from the same voxel at $\Delta = 150$ ms and $\Delta = 900$ ms—their integrals are the same because the fluid content of the voxel is the same in both cases. It can be seen that the local propagators assume various shapes that are different from the shape of the global propagator. For example, in Fig. 9(b), the propagator is taken from a region where the fluid is stagnant—the propagators are symmetric Gaussians centered around zero displacement. The propagator for $\Delta = 900$ ms is broader due to additional self-diffusion compared to the one at $\Delta = 150$ ms. At short timescales, most of the local propagators have this simple, Gaussian shape centered around zero displacement, because much of the water in the rock is stagnant as was shown in Fig. 3(a). Figure 9(c) shows local propagators taken for a voxel in which there is significantly different behavior at the two observation times. At $\Delta = 150$ ms, the propagator is clearly indicative of stagnant water; however, for $\Delta = 900$ ms the mean displacement has clearly shifted to a positive value. This effect may be counterintuitive, because the mean displacement between the total propagators for $\Delta = 150$ ms and 900 ms is the same. However, the shift in mean displacement on a local level is expected since in the limit of very long Δ, the local propagators must resemble the global propagator due to fluid mixing throughout the rock sample; mixing takes place due

to self-diffusion and additional dispersion between voxels. Therefore, the mean displacement within a single voxel must change with Δ. The propagators shown in Figs. 9(d)–9(f) are examples where the propagator is bimodal at $\Delta = 150$ ms, indicating that those single voxels contain two fractions of fluid that are associated with two different flow rates, i.e., two fluid streams that have not diffusively exchanged. At the longer observation time, diffusive exchange has taken place, and the propagators have merged into unimodal but skewed distributions.

We can exploit the fact that in the limit of very long Δ, where complete mixing will have taken place, all local propagators must be identical, to track the progress of mixing on a local level from the spatially resolved propagator. To capture the essential properties of the local propagators, $\bar{P}(\mathbf{R}, \Delta)$, as simple statistical descriptors, we extract the mean (μ) and standard deviation (σ) of displacement. The mean is given by

$$\mu = \frac{\int \bar{P}(\mathbf{R}, \Delta)\, \mathbf{R} d\mathbf{R}}{\int \bar{P}(\mathbf{R}, \Delta) d\mathbf{R}}, \tag{3}$$

and the standard deviation is given by the square root of the variance of the propagator as

$$\sigma = \sqrt{\frac{\int \bar{P}(\mathbf{R}, \Delta)(\mathbf{R} - \mu)^2 d\mathbf{R}}{\int \bar{P}(\mathbf{R}, \Delta) d\mathbf{R}}}, \tag{4}$$

where $\mathbf{R}$ is the displacement over observation time Δ.

Figure 10 shows two 2D histograms for $\Delta = 150$ ms [Fig. 10(a)] and $\Delta = 900$ ms [Fig. 10(b)], wherein the mean and standard deviation of all local propagators in the rock sample are collected. Both mean and standard deviation
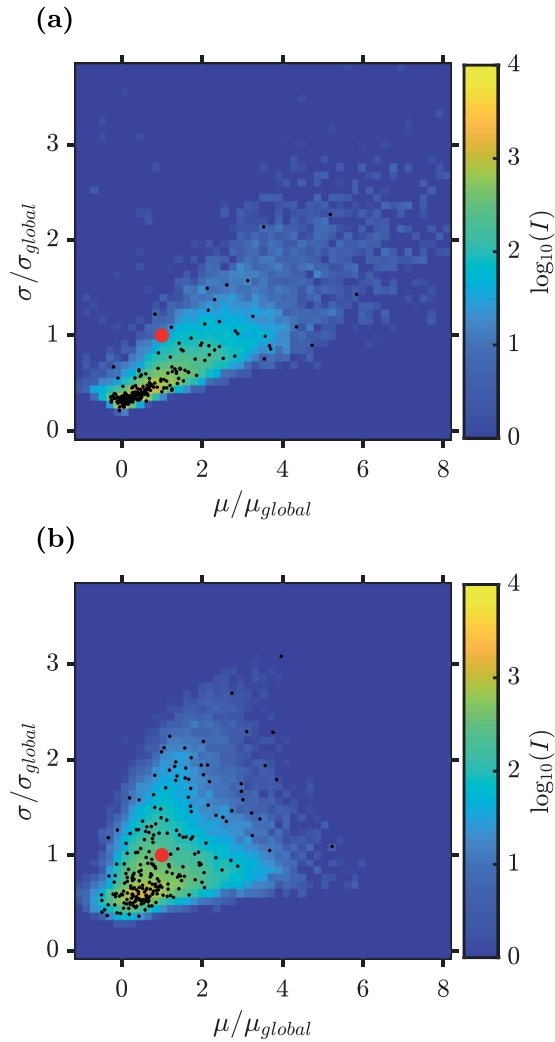
(a)

(b)

FIG. 10. 2D histograms showing the mean and standard deviation of all local propagators in the rock, for (a) $\Delta = 150\,\text{ms}$ and (b) $\Delta = 900\,\text{ms}$. Both mean and standard deviation are rescaled using the values calculated for the global propagator at the given Δ. The color scale corresponds to the $\log_{10}$ of the total integral I of all the propagators within each bin. The black dots show the exact position of 0.1% of the total number of local propagators, randomly picked from the data set. The red dot indicates the position $\mu/\mu_{\text{global}} = 1$, $\sigma/\sigma_{\text{global}} = 1$ for reference.

are rescaled using the values calculated for the global propagator. The red dot indicates the position $\mu/\mu_{\text{global}} = 1$ and $\sigma/\sigma_{\text{global}} = 1$, onto which all propagators should converge at long Δ; at long timescales, the flow rate is negligible, and the propagators will be fully dominated by self-diffusion. The color intensities, I, in both histograms represent the total sum of fluid in each position (bin) of μ/μ_{global} and $\sigma/\sigma_{\text{global}}$. The exact positions of 0.1% of the local propagators randomly picked from the data set are also shown, indicated by the black dots, which helps to guide the eye.

For $\Delta = 150\,\text{ms}$ [Fig. 10(a)], it is seen that many propagators are concentrated close to $\mu/\mu_{\text{global}} = 0$ and $\sigma/\sigma_{\text{global}} = 0.3$. All these propagators are located within stagnation zones and have not had sufficient time to couple into the flow through diffusive exchange, so that the propagators are purely

self-diffusive, as in Fig. 9(b). The tail of the distribution extends towards large values of μ/μ_{global} and $\sigma/\sigma_{\text{global}}$; these data are associated with the propagators from within or close vicinity to the flow channels identified in Fig. 3(a) and 8(b). At this relatively short timescale, the molecules in these areas have not yet significantly exchanged with the water in the stagnation zones. The expectation value for self-diffusive displacement of a fluid molecule equals $\sqrt{2D\Delta}$, which equals 24 μm for water after 150 ms and 60 μm after 900 ms. The effects of this additional mobility can be seen in Fig. 10(b). The distribution of points around $\mu/\mu_{\text{global}} = 1$ has become significantly narrower, while at the same time, the distribution of $\sigma/\sigma_{\text{global}}$ has shifted towards higher values. Many of the propagators, which represented stagnant water at $\Delta = 150\,\text{ms}$, have shifted towards $\mu/\mu_{\text{global}} = 1$ and $\sigma/\sigma_{\text{global}} = 1$. At this longer timescale, the effects of Taylor dispersion [58] are seen whereby molecules which were in stagnant zones at short timescales will have moved across the streamlines of the flowing zones at longer timescales. This mixing between the fluid molecules in flowing and stagnant zones within a single voxel leads to the local flow propagator identifying greater dispersion than the global propagator. However, as was already evident from the global propagator at $\Delta = 900\,\text{ms}$, which was not Gaussian in shape, complete mixing has not yet occurred, and has not been observed in heterogeneous carbonate rocks even at observation times of several seconds [50].

A final look at the spatially resolved propagator is aimed at answering the question whether the data can be used to determine which voxel size equals a representative elementary volume (REV) [5] for the observed flow phenomena in the rock. As is seen in the flow maps and spatially resolved propagators in Figs. 7 and 8, flow pathways are sparsely distributed across an axial cross section of the rock and therefore the question arises whether the flow properties of this rock have already averaged out at a 4-mm scale. In the context of spatially resolved propagators, a REV can be identified by finding the smallest volume element which has an associated propagator that is not significantly different from the total propagator of the entire region of interest. For this analysis, a cubic volume containing 24^3 voxels (total volume $2.25^3\,\text{mm}^3$) was selected from a region within the rock. The propagator with $\Delta = 150\,\text{ms}$ is used because at this timescale, the flow field is less dominated by diffusion than for the experiment at $\Delta = 900\,\text{ms}$. This volume was successively coarse-grained to an array containing 4^3, 2^3 voxels, and finally to a single volume. Mean and standard deviation were calculated for each of the voxels in the different data sets and rescaled using the "global" result obtained for the single volume (voxel); the results of this analysis are shown in Fig. 11. It is seen that the going from the smallest voxel size (black dots) to the global result at $\mu/\mu_{\text{global}} = \sigma/\sigma_{\text{global}} = 1$ (blue-green diamond), the distributions of mean and standard deviation become increasingly narrow and approach the global result. Nevertheless, even at the second lowest resolution (blue inverted triangles, 2^3 voxels), there still exists significant variation of μ/μ_{global} and $\sigma/\sigma_{\text{global}}$ between the different voxels, relative to the global result (blue-green diamond). It is therefore likely that the global result does not yet constitute an REV for this sample of Ketton rock. Since spatial resolution
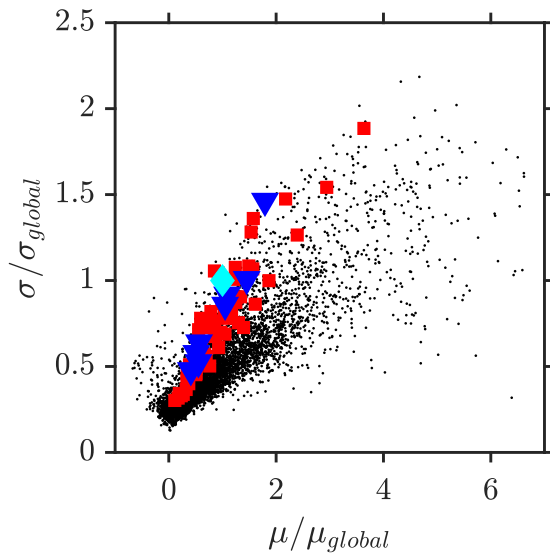
FIG. 11. Rescaled mean μ/μ_{global} and standard deviation $\sigma/\sigma_{\text{global}}$ of per-voxel propagators at different coarse-grained spatial resolutions. The highest resolution of 94 μm (●) equals that of the acquired data. The acquired data have been coarse-grained to 562 μm (■), 1.125 mm (▼) and 2.25 mm (◆) isotropic spatial resolutions. The result for 2.25 mm spatial resolution represents a single voxel and is therefore found at position (1,1).

and displacement resolution can be chosen independently in the acquisition of spatially resolved propagators, it would also be possible to carry out this analysis on larger rock core plugs at coarser spatial resolutions without significantly increasing the image acquisition time, in order to identify flow-characterizing REVs at a much larger length scale.

V. CONCLUSIONS

In this paper, quantitative, 3D velocity maps and spatially resolved propagators acquired at a pore-scale resolution have been presented and analyzed to study flow-structure correlations for a single-phase flow through a 4-mm-diameter Ketton limestone rock core plug. The high spatial resolution of flow MRI achieved in this work enabled the detail of flow structure in the rock to be studied.

First, a compressed sensing PGSE-RARE sequence was used to acquire quantitative, 3D spatially resolved velocity maps at 35 μm spatial resolution, which is about one or-

der of magnitude higher than has been reported using more conventional MRI flow methods. Using 3D visualization and quantitative analysis of the pore-scale MRI flow fields, it was shown that flow in Ketton limestone rock is carried by only a few flow channels which mainly consist of large pores; it was found that 53% of the flow is carried by just 10% of the pores. Furthermore, it was demonstrated how coregistration and visualization of MRI flow fields and μCT images can be exploited to correlate complex flow phenomena, such as backflow, with the microstructural characteristics of the rock. In particular, the correlation of local flow velocities with pore size and coordination number was studied. It was also shown that the structure-flow characteristics of Ketton rock were well approximated by flow through a packing of spheres.

Second, an undersampled APGSTE-RARE experiment was used to acquire spatially resolved propagators at 94 μm spatial resolution. Two 3D spatially resolved propagators, containing 331 776 voxels, each of which contains a local propagator, were acquired using observation times of 150 ms and 900 ms. Based on the segmentation of the global propagator acquired at the shortest observation time, stagnant and flowing water images were generated and coregistered with the high-resolution μCT image of Ketton rock. This analysis demonstrated that stagnant and flowing water coexists in some large pores. A comparison between the propagators acquired at the short and long observation times enabled study of fluid dispersion at the pore scale. Flow dispersion was observed by quantifying the changes in mean and standard deviation of each of the local propagators as a function of observation time.

Although these MRI techniques were developed for studying rock samples in the context of Digital Rock technology, they are not limited to only this application, but are generic and can be used to obtain flow information in any porous material. Future work will extend the use of these flow MRI methods to study rock dissolution processes for CCS applications and will also be used as a basis for developing multiphase flow MRI techniques.

[1] H. Andrä, N. Combaret, J. Dvorkin, E. Glatt, J. Han, M. Kabel, Y. Keehm, F. Krzikalla, M. Lee, C. Madonna *et al.*, Comput. Geosci. **50**, 25 (2013).

[2] H. Andrä, N. Combaret, J. Dvorkin, E. Glatt, J. Han, M. Kabel, Y. Keehm, F. Krzikalla, M. Lee, C. Madonna *et al.*, Comput. Geosci. **50**, 33 (2013).

[3] M. J. Blunt, B. Bijeljic, H. Dong, O. Gharbi, S. Iglauer, P. Mostaghimi, A. Paluszny, and C. Pentland, Adv. Water Resour. **51**, 197 (2013).

[4] N. Saxena, R. Hofmann, F. O. Alpak, S. Berg, J. Dietderich, U. Agarwal, K. Tandon, S. Hunter, J. Freeman, and O. B. Wilson, Adv. Water Resour. **109**, 211 (2017).

[5] N. Saxena, A. Hows, R. Hofmann, F. O. Alpak, J. Freeman, S. Hunter, and M. Appel, Adv. Water Resour. **116**, 127 (2018).

[6] N. P. Ramskill, A. J. Sederman, M. D. Mantle, M. Appel, H. de Jong, and L. F. Gladden, Transp. Porous Media **121**, 15 (2018).

[7] J. J. Dechter, R. A. Komoroski, and S. Ramaprasad, J. Magn. Reson. **93**, 142 (1991).

[8] K. Karlsons, D. W. de Kort, A. J. Sederman, M. D. Mantle, H. de Jong, M. Appel, and L. F. Gladden, J. Microsc. **276**, 63 (2019).

[9] D. Xiao and B. J. Balcom, J. Magn. Reson. **220**, 70 (2012).

[10] K. Romanenko, D. Xiao, and B. J. Balcom, J. Magn. Reson. **223**, 120 (2012).

[11] L. F. Gladden and A. J. Sederman, J. Magn. Reson. **229**, 2 (2013).

[12] L. Huang, G. Mikolajczyk, E. Küstermann, M. Wilhelm, S. Odenbach, and W. Dreher, J. Magn. Reson. **276**, 103 (2017).

[13] D. W. de Kort, S. A. Hertel, M. Appel, H. de Jong, M. D. Mantle, A. J. Sederman, and L. F. Gladden, Magn. Reson. Imaging **56**, 24 (2019).

[14] N. P. Ramskill, I. Bush, A. J. Sederman, M. D. Mantle, M. Benning, B. C. Anger, M. Appel, and L. F. Gladden, J. Magn. Reson. **270**, 187 (2016).

[15] M. Lustig, D. Donoho, and J. M. Pauly, Magn. Reson. Med. **58**, 1182 (2007).

[16] H. P. Menke, C. A. Reynolds, M. G. Andrew, J. P. Pereira Nunes, B. Bijeljic, and M. J. Blunt, Chem. Geol. **481**, 27 (2018).

[17] M. Andrew, B. Bijeljic, and M. J. Blunt, Int. J. Greenh. Gas Control **22**, 1 (2014).

[18] D. W. de Kort, A. Reci, N. P. Ramskill, M. Appel, H. de Jong, M. D. Mantle, A. J. Sederman, and L. F. Gladden, J. Magn. Reson. **295**, 45 (2018).

[19] E. O. Stejskal and J. E. Tanner, J. Chem. Phys. **42**, 288 (1965).

[20] S. Berg, H. Ott, S. A. Klapp, A. Schwing, R. Neiteler, N. Brussee, A. Makurat, L. Leu, F. Enzmann, J.-O. Schwarz *et al.*, Proc. Natl. Acad. Sci. USA **110**, 3755 (2013).

[21] M. Benning, L. F. Gladden, D. J. Holland, C.-B. Schönlieb, and T. Valkonen, J. Magn. Reson. **238**, 26 (2014).

[22] P. T. Callaghan, *Translational Dynamics and Magnetic Resonance: Principles of Pulsed Gradient Spin Echo NMR* (Oxford University Press, Oxford, 2011).

[23] E. Fukushima, Annu. Rev. Fluid Mech. **31**, 95 (1999).

[24] J. Hennig, A. Nauerth, and H. Friedburg, Magn. Reson. Med. **3**, 823 (1986).

[25] D. J. Holland, D. M. Malioutov, A. Blake, A. J. Sederman, and L. F. Gladden, J. Magn. Reson. **203**, 236 (2010).

[26] M. H. Sankey, D. J. Holland, A. J. Sederman, and L. F. Gladden, J. Magn. Reson. **196**, 142 (2009).

[27] R. M. Cotts, M. J. R. Hoch, T. Sun, and J. T. Markert, J. Magn. Reson. **83**, 252 (1989).

[28] T. W. J. Scheenen, F. J. Vergeldt, C. W. Windt, P. A. de Jager, and H. Van As, J. Magn. Reson. **151**, 94 (2001).

[29] V. A. Morozov, USSR Comput. Math. Math. Phys. **6**, 242 (1966).

[30] S. Beucher and F. Meyer, in *Mathematical Morphology in Image Processing*, edited by E. R. Dougherty (Marcel Dekker, New York, 1993), pp. 433–481.

[31] H. Dong and M. J. Blunt, Phys. Rev. E **80**, 036307 (2009).

[32] J. P. W. Pluim, J. B. A. Maintz, and M. A. Viergever, IEEE T. Med. Imaging **22**, 986 (2003).

[33] C. Studholme, D. L. G. Hill, and D. J. Hawkes, Pattern Recognit. **32**, 71 (1999).

[34] Thermo Scientific Avizo Software 9: User's Guide (n.d.).

[35] C. E. Duchon, J. Appl. Meteorol. **18**, 1016 (1979).

[36] A. J. Sederman, M. L. Johns, P. Alexander, and L. F. Gladden, Chem. Eng. Sci. **53**, 2117 (1998).

[37] M. L. Johns, A. J. Sederman, A. S. Bramley, L. F. Gladden, and P. Alexander, AIChE J. **46**, 2151 (2000).

[38] B. Bijeljic, P. Mostaghimi, and M. J. Blunt, Phys. Rev. Lett. **107**, 204502 (2011).

[39] A. J. Katz and A. H. Thompson, Phys. Rev. B **34**, 8179 (1986).

[40] C. B. Shah and Y. C. Yortsos, AIChE J. **41**, 1099 (1995).

[41] R. B. Saeger, L. E. Scriven, and H. T. Davis, J. Fluid Mech. **299**, 1 (1995).

[42] R. S. Maier, D. M. Kroll, Y. E. Kutsovsky, H. T. Davis, and R. S. Bernard, Phys. Fluids **10**, 60 (1998).

[43] Y. E. Kutsovsky, L. E. Scriven, H. T. Davis, and B. E. Hammer, Phys. Fluids **8**, 863 (1996).

[44] X. Ren, S. Stapf, and B. Blümich, Chem. Eng. Technol. **28**, 219 (2005).

[45] A. J. Sederman, M. L. Johns, A. S. Bramley, P. Alexander, and L. F. Gladden, Chem. Eng. Sci. **52**, 2239 (1997).

[46] A. J. Sederman and L. F. Gladden, Magn. Reson. Imaging **19**, 339 (2001).

[47] P. R. Thomson, A. Aituar-Zhakupova, and S. Hier-Majumder, Front. Earth Sci. **6**, 1 (2018).

[48] U. M. Scheven and P. N. Sen, Phys. Rev. Lett. **89**, 254501 (2002).

[49] L. Lebon, J. Leblond, and J. P. Hulin, Phys. Fluids **9**, 481 (1997).

[50] B. S. Akpa, D. J. Holland, A. J. Sederman, M. L. Johns, and L. F. Gladden, J. Magn. Reson. **186**, 160 (2007).

[51] B. Manz, L. F. Gladden, and P. B. Warren, AIChE J. **45**, 1845 (1999).

[52] B. Manz, P. Alexander, and L. F. Gladden, Phys. Fluids **11**, 259 (1999).

[53] D. A. Verganelakis, J. Crawshaw, M. L. Johns, M. D. Mantle, U. Scheven, A. J. Sederman, and L. F. Gladden, Magn. Reson. Imaging **23**, 349 (2005).

[54] U. M. Scheven, D. Verganelakis, R. Harris, M. L. Johns, and L. F. Gladden, Phys. Fluids **17**, 117107 (2005).

[55] U. M. Scheven, J. G. Seland, and D. G. Cory, Phys. Rev. E **69**, 021201 (2004).

[56] P. M. Singer, J. Mitchell, and E. J. Fordham, J. Magn. Reson. **270**, 98 (2016).

[57] K. J. Packer, S. Stapf, J. J. Tessier, and R. A. Damion, Magn. Reson. Imaging **16**, 463 (1998).

[58] G. Taylor, Proc. R. Soc. London A **219**, 186 (1953).